ADVANCED
FUNCTIONAL
MATERIALS

# Supporting Information

for *Adv. Funct. Mater.*, DOI 10.1002/adfm.202419594

# The Out-of-Plane C—S Bonds Boosting Reversible Redox in Copper Sulfide Cathodes for Ultradurable Magnesium Battery

*Qin Su, Weixiao Wang, Jiajun Chen, Juan Ji, Wenwen Wang, Wen Ren*, Lei Zhang*, Jun Xie* and Qinyou An**

Supporting Information

# The Out-of-Plane C-S Bonds Boosting Reversible Redox in Copper Sulfide Cathodes for Ultradurable Magnesium battery

*Qin Su, Weixiao Wang, Jiajun Chen, Juan Ji, Wenwen Wang, Wen Ren,* Lei Zhang,* Jun Xie,* Qinyou An**

## Experimental section

### Preparation of Material

Preparation of CuS@GO: All the reagents using in the synthesis were analytical grade and purchased from the Aladdin reagent Co., Ltd. First, 5 mmol of $CuCl_2 \cdot H_2O$ and 14.48 mmol of tris-aminomethane ($C_4H_{11}NO_3$, THAM) were dissolved in 60 mL of a graphene oxide solution (1 mg/mL) by stirring for 10 minutes. Then, 10 mL of 2 M ammonia solution was added and the mixture was stirred for another 10 minutes. Subsequently, 10 mL of 1 M NaOH was incorporated and stirred for an additional 10 minutes. Afterward, 6 mL of 1 M thiourea ($NH_2CSNH_2$) solution was introduced and stirred for 10 minutes. This was followed by the addition of deionized water, bringing the final volume to 150 mL. The solution was then left undisturbed for 3 hours to precipitate. The resulting precipitate was washed multiple times with deionized water and ethanol, and subsequently dried at 60 °C.

Preparation of CuS@rGO: First, 5 mL of hydrazine hydrate ($N_2H_4 \cdot H_2O$, 80%) was added to 50 mL of deionized water, stirred for 5 minutes to ensure thorough mixing. Then, 200 mg of CuS@GO powder was introduced into the prepared hydrazine hydrate solution and stirred for an additional 5 minutes. The mixture was then heated in a water bath for 3 hours. After cooling, the solution was washed alternately with deionized water and ethanol three times, followed by vacuum drying at 60 °C for 6 hours. The graphene solution in the synthesis step was replaced with deionized water, and the above steps were repeated to obtain a pure CuS sample.[1]

## Preparation of electrolytes

The MPFB electrolyte is synthesized and configured according to the work of predecessors, and the specific steps are as follows. The MPFB electrolyte is synthesized and configured according to the work of predecessors.[2] In an argon filled glovebox, $AlCl_3$ (2 mmol) was dissolved in 5 mL dry DME. Then, $Mg(PFTB)_2$ (1 mmol) was added into the above solution. After magnetic stirring at room temperature for minutes, a clear solution was obtained. Finally, $MgCl_2$ (1 mmol) was added to the above solution and stirred at room temperature for 12 h to obtain a clear and colorless solution, which is MPFB electrolyte.

## Material characterizations

The morphology of the samples was characterized using field-emission scanning electron microscopy (SEM, JSM-7100F) and transmission electron microscopy (TEM, JEM-1400Plus). X-ray diffraction (XRD, Bruker D8 Discover), Raman spectrometry (Lab RAM HR-Evolution, 532 nm) and X-ray photoelectron spectroscopy (XPS, AXIS SUPRA) were carried out to investigate the structure and chemical composition of the samples. The composition of SEI was acquired by time-of-flight secondary-ion mass spectrometry (TOF-SIMS, nano TOFIII).

## Electrochemical measurements

The electrochemical properties of the as-prepared samples were measured using coin cells (CR2016). An electrode slurry consisting of 70 wt.% as-prepared samples, 20 wt.% carbon black, and 10 wt.% polyvinylidene fluoride (PVDF) in N-methly-2-pyrrolidone (NMP) solvent was coated onto carbon paper and then dried overnight at 60 °C under vacuum. The as-prepared electrode was punched into a 10 mm disk and paired with a magnesium metal counter electrode separated by a glass fiber film (Whatman, GF/D). All the electrochemical measurements including cyclic voltammetry (CV), galvanostatic charge-discharge (GCD), electrochemical impedance spectroscopy (EIS) and galvanostatic intermittent titration technique (GITT) were conducted with LAND battery testing systems.

## DFT Calculations

All computations were performed using the Vienna Ab initio Simulation Package (VASP-5.4.4).[3,4] The Generalized Gradient Approximation (GGA) with the Perdew-Burke-Ernzerhof (PBE)[5] exchange-correlation functional and the Projector Augmented-Wave (PAW)[6] method were employed. Geometry optimizations were conducted using the Conjugate Gradient (CG) method, with a plane-wave cutoff energy set at 500 eV. The convergence criteria for structural optimizations were set to 0.02 eV/Å. The total energy convergence was defined at $10^{-6}$ eV. For the k-point sampling, a 6×6×1 Monkhorst–Pack k-point grid was used during the geometry optimizations, while a denser 18×18×1 grid was employed for the electronic structure calculations. Heterostructures of graphene and CuS were constructed with the (001) surface of CuS using a 2×2 supercell. Graphene was modeled as a bilayer using a 3×3 supercell, ensuring a lattice mismatch of less than 5%. A vacuum layer exceeding 15 Å in thickness was added to prevent interactions between periodic images. Van der Waals interactions were incorporated using the DFT-D3 method to accurately represent dispersion forces.[7] Crystallographic structures and visualizations were generated using VESTA software.[8]

The bonding strength between two materials can be quantitatively described using the bonding energy, defined by the following equation:

$$E_{\mathrm{bind}} = (E_{\mathrm{AB}} - E_A - E_B)/S$$

Where $E_{AB}$ is the total energy of the composite structure of materials A and B, $E_A$ and $E_B$ are the energies of the individual A and B structures, respectively. S is the area of the interface.

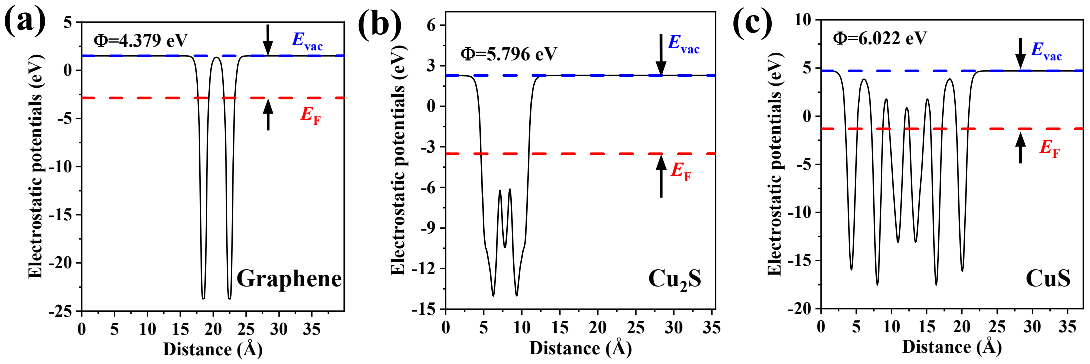

Figure S1 Work functions of (a) graphene, (b) $Cu_2S$, and (c) CuS

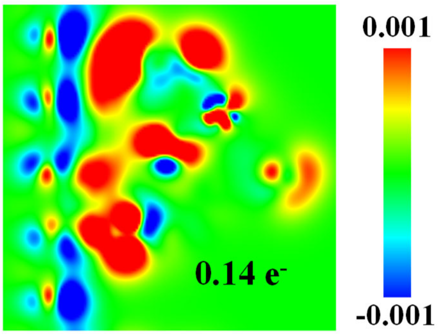

Figure S2 Cross-sectional diagram of $Cu_2S$ (red) and graphene (blue) differential charge.

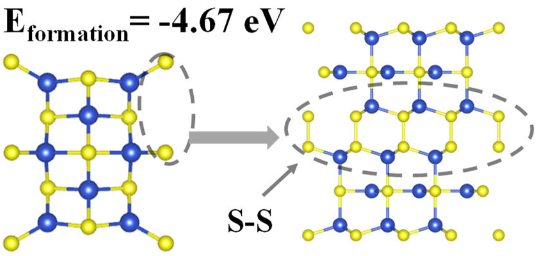

Figure S3 In the absence of a C-S bond, the S-S bond formation energy.

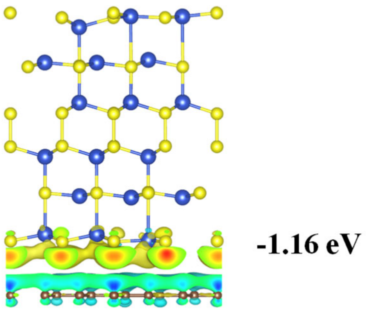

Figure S4 Calculation of CuS and graphene interfacial interactions

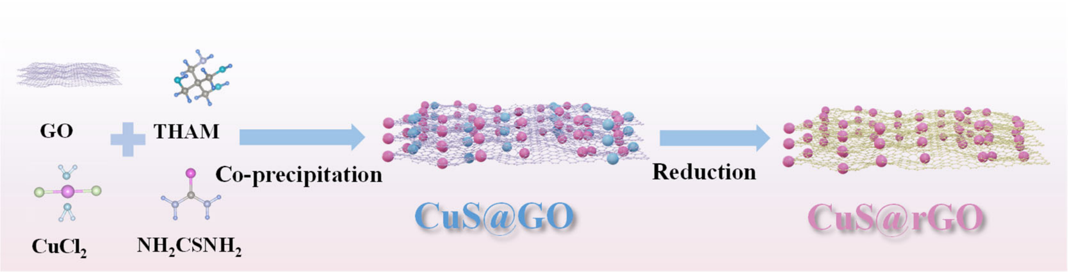

**Figure S5 Schematic illustration of CuS@G fabrication.**

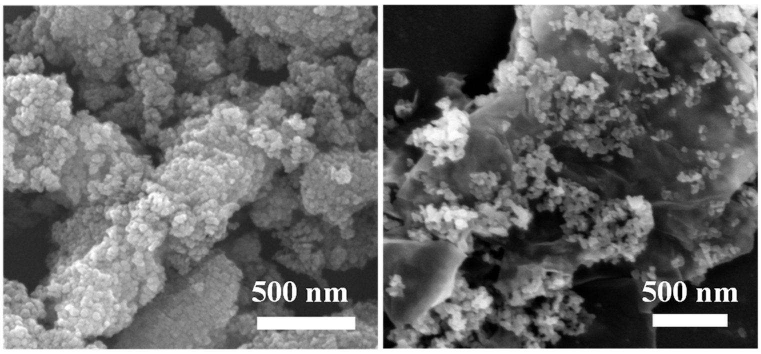

**Figure S6 FESEM image of CuS and CuS@G.**

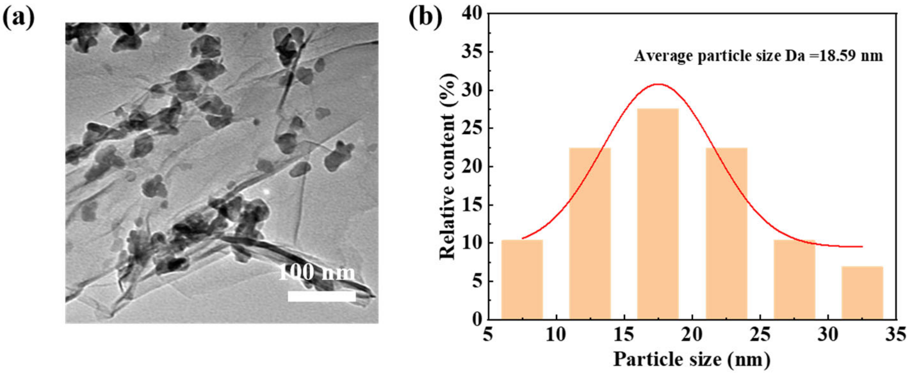

**Figure S7. (a) TEM images of CuS@G. (b) Particle size distribution of CuS@G.**

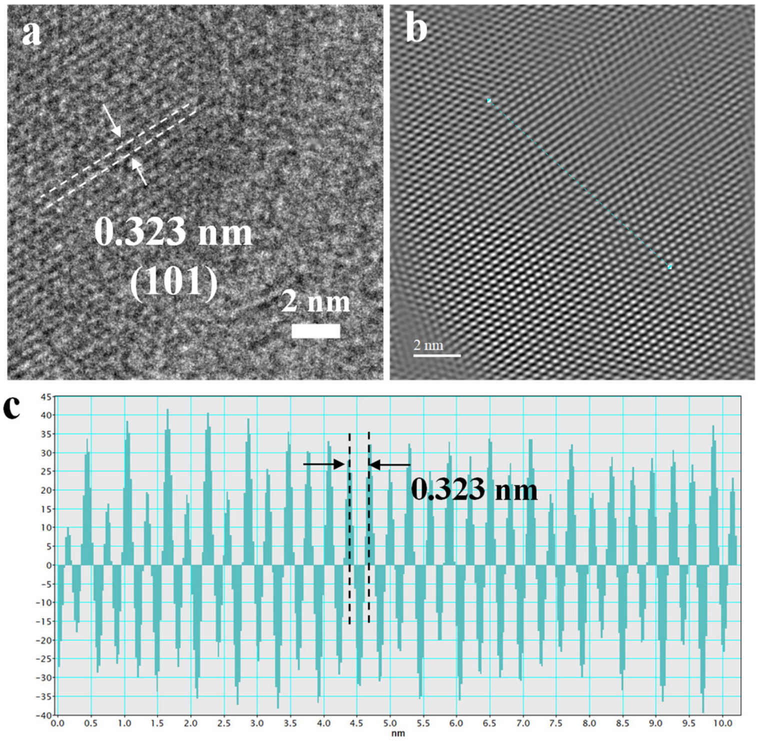

Figure S8 (a)Partial enlargement of the white box in Figure 2b. (b) Lattice fringe Fourier transform image. (c) Measurement of lattice spacing.

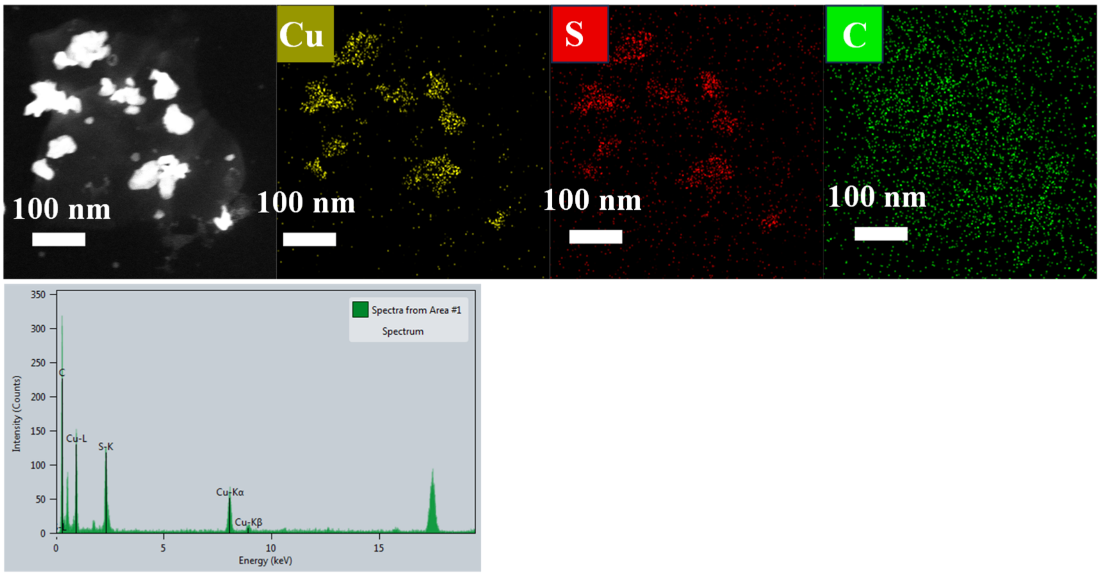

Figure S9 EDX mapping images (Cu、S、C).

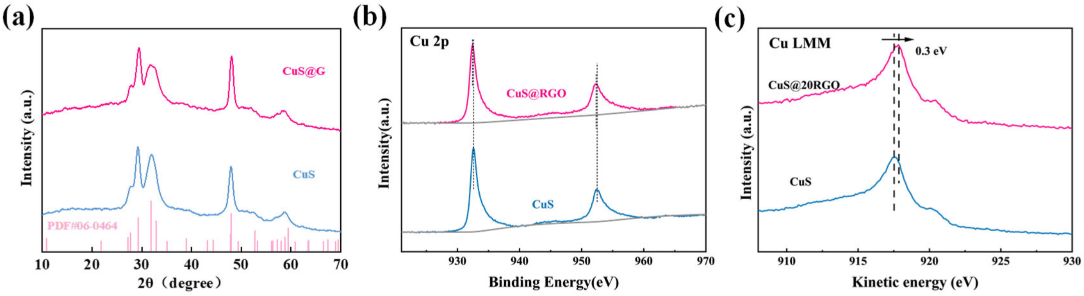

**Figure S10 (a) XRD patterns. High-resolution XPS spectra: (b) Cu 2p and (c) Cu LMM.**

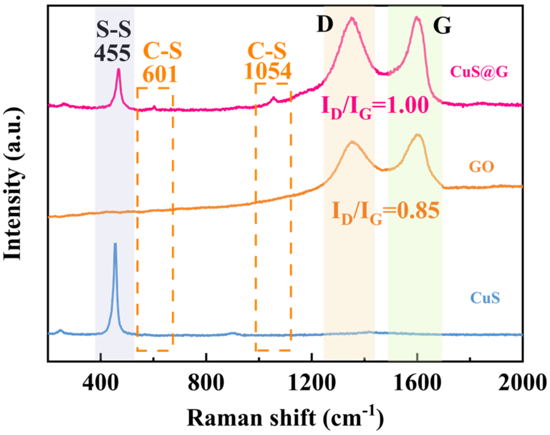

**Figure S11 Raman spectra of pure CuS, reduced graphene and CuS@G.**

To demonstrate that the new peaks at 601 and 1054 cm$^{-1}$ observed in the CuS@G sample do not originate from graphene, we measured the Raman spectrum of graphene oxide (GO). The results showed no peaks at 601 and 1054 cm$^{-1}$ in the GO spectrum, confirming that the C–S bond was successfully introduced into the CuS structure (**Figure S11**). Moreover, the D-to-G peak intensity ratio of GO is 0.85, which is lower than the 1.00 ratio observed in CuS@G, indicating that the graphene oxide was effectively reduced.

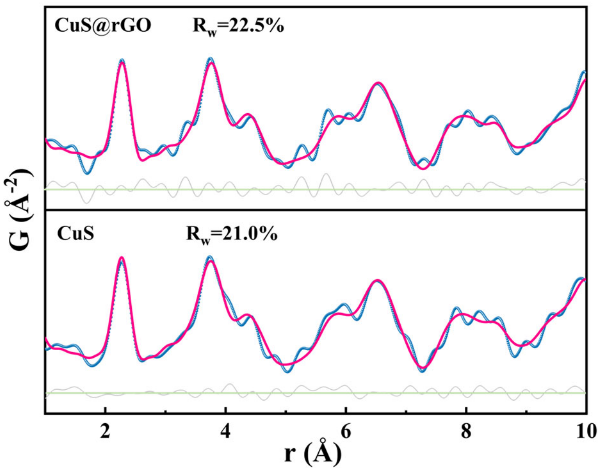

**Figure S12 The results of the refinement of the pair distribution function.**

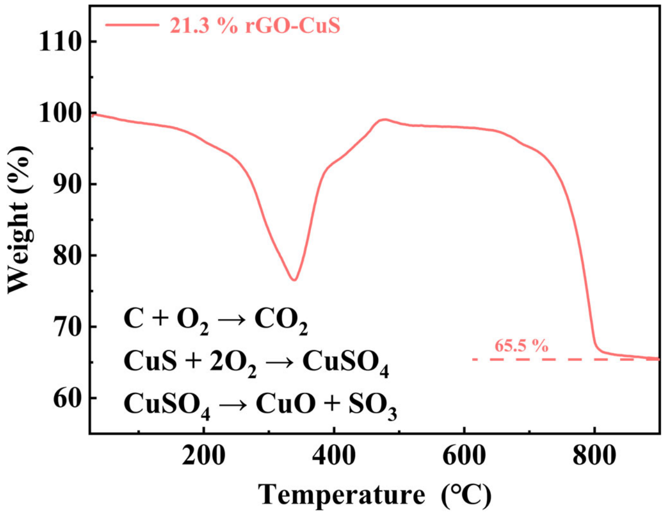

**Figure S13 Thermogravimetric curves (Air).**

The TGA responses of the CuS@G found the mass losses in the temperature range (150–300 °C). Losses in this range were previously attributed to the oxidation of amorphous carbon and the evolution of $SO_2$ gas as a by-product during the conversion of CuS to $Cu_2S$ (Equation S1).

$$2CuS + O_2 \rightarrow Cu_2S + SO_2 \quad (S1)$$

Once all CuS has been converted to $Cu_2S$, the $Cu_2S$ begins to transform into $Cu_2O$, causing further mass loss (Equation S2). There is a slight mass drop present in the $Cu_2S$ TGA curve which is attributed to the oxidation of the carbon. From 370 °C, sample exhibits a mass uptake, with the uptake percentages caused by the varying amounts of

$Cu_xS$ being present in the sample. This response is due to the conversion of $Cu_2S$ to the intermediate copper sulphate (Equation S3). $CuO{\cdot}CuSO_4$ is stable up to approx 650 °C, with the mass drop starting at 650–700 °C signaling the decomposition of the $CuO{\cdot}CuSO_4$ to CuO (Equation S4 and Equation S5).

$$Cu_2S + 1.5\ O_2 \rightarrow Cu_2O + SO_2 \qquad (S2)$$

$$Cu_2O + SO_2 + O_2 \rightarrow CuO{\cdot}CuSO_4 \qquad (S3)$$

$$CuO{\cdot}CuSO_4 \rightarrow 2CuO + SO_2 + 0.5\ O_2 \qquad (S4)$$

The TGA curves stable again between 760 °C with a resulting weight loss of 65.5%. Based on the above equation, it can be calculated that the graphene content of CuS@G is approximately 20%.

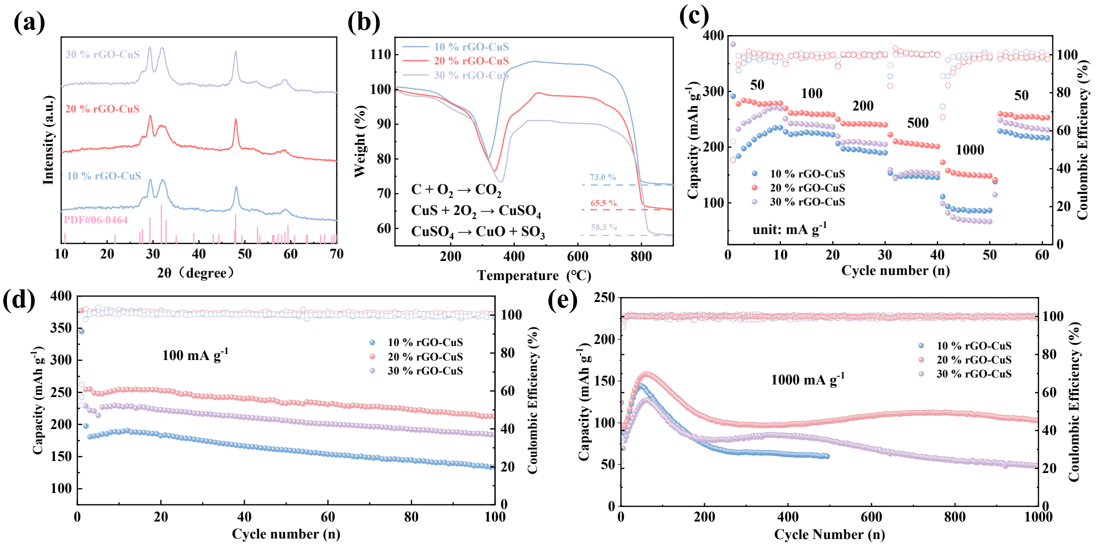

**Figure S14. (a) XRD pattern. (b) Thermogravimetric (TG) curve. (c) Rate capabilities at current densities of 50 to 1000 mA g$^{-1}$. (d) Cycling performance and Coulombic efficiencies at current densities of 100 mA g$^{-1}$. (e) Cycling performance and Coulombic efficiencies at current densities of 1000 mA g$^{-1}$.**

Following the same preparation method outlined in the main text, we synthesized three copper sulfide (CuS) cathodes with varying graphene content by using graphene solutions at three different concentrations (0.5, 1, and 1.5 mg/ml). XRD analysis (**Figure S14**a) confirmed that all samples were in the covellite phase (CuS, JCPDS No.

06-0464). Thermogravimetric analysis (TGA) was conducted under an argon atmosphere to ascertain the graphene content, revealing approximate values of 10%, 20%, and 30%, respectively. (**Figure S14**b).

Following sample preparation, electrochemical tests were conducted to assess the impact of graphene content on performance. **When the graphene content is low (10%), fewer C-S bonds form between the small CuS particles and graphene, thereby limiting the CuS available for reversible phase transitions.** This leads to a reduced capacity, as the active material transitions solely to $Cu_2S$. At an optimal graphene content of 20%, the rate performance is maximized, achieving a capacity of 280 mAh $g^{-1}$ at a current density of 50 mA $g^{-1}$ (**Figure S14**c). Even at an elevated current density of 1 A $g^{-1}$, a capacity of 160 mAh $g^{-1}$ (57% of the initial value) is retained. Conversely, when the graphene content is higher (30%), both capacity and rate performance exhibit marked declines. This results from the limited surface area of CuS, which can only form C-S bonds with a finite amount of graphene to facilitate reversible phase transitions and enhance capacity. **Excess graphene that does not bond with CuS contributes minimally to capacity, leading to a reduction in reversible capacity.** Extended long-cycle testing of the sample demonstrated its outstanding capacity and improved long-term cycling stability (**Figure S14**d and e).

**Overall, with a graphene content of 20%, more C–S bonds can form between copper sulfide and graphene, while the amount of unbound graphene in the system is minimized, resulting in optimal performance.**

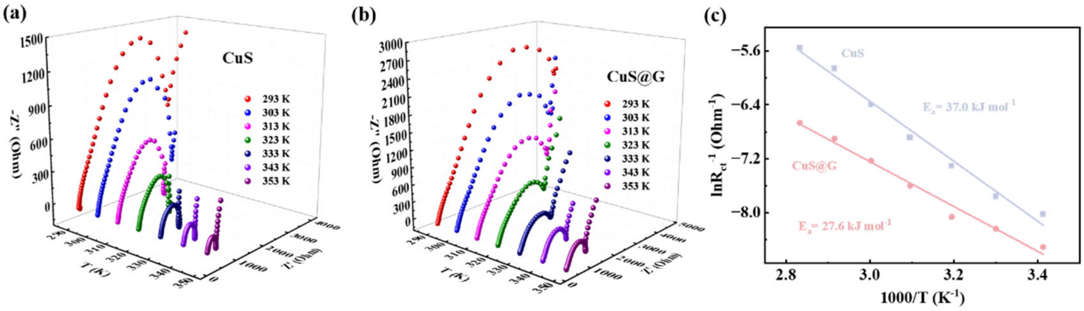

**Figure S15** EIS of (a) CuS and (b) CuS@G at varied temperatures. (c) The related activation energy of CuS and CuS@G.

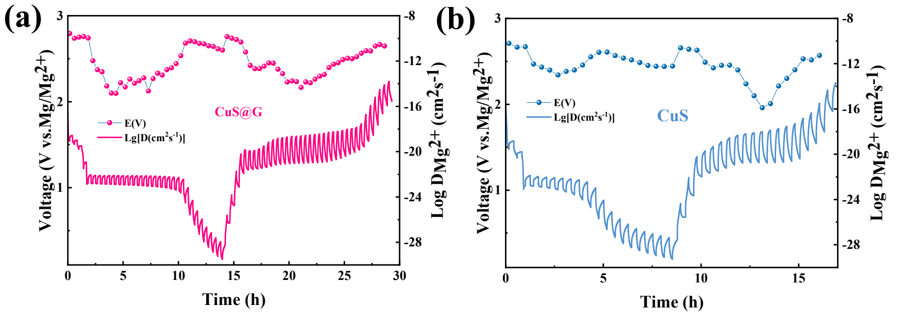

**Figure S16** GITT curves and the corresponding $Mg^{2+}$ diffusion coefficients of (a) CuS@G and (b) pure CuS.

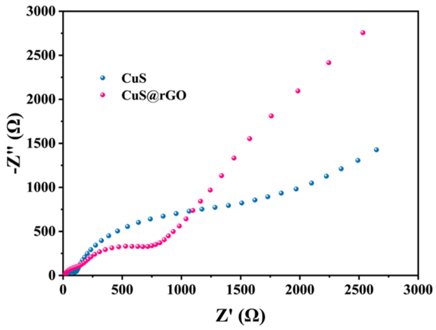

**Figure S17** Nyquist plots of as-obtained (b) CuS@G and (b) CuS.

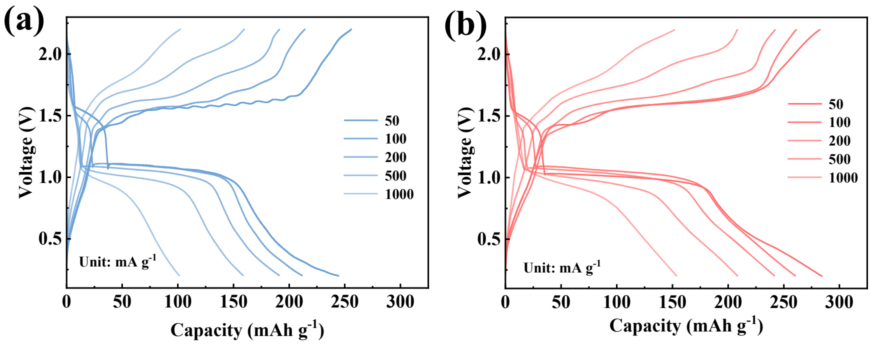

**Figure S18 Charge-discharge curves of CuS@G and CuS at different current densities.**

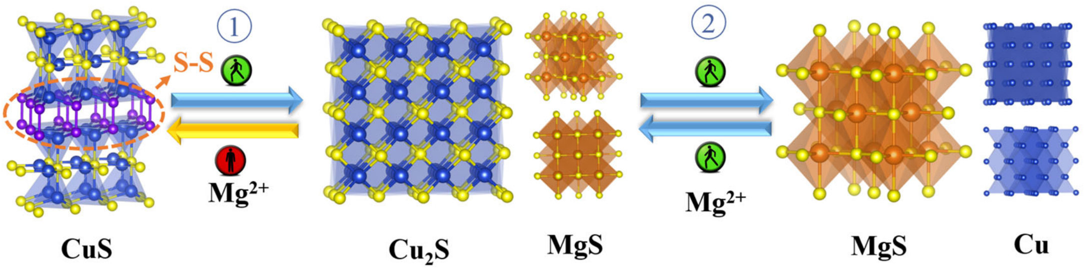

**Figure S19 Schematic diagram of changes in the cyclic crystal structure of CuS**

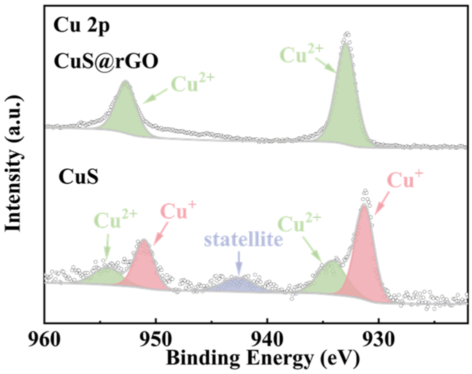

**Figure S20 XPS spectra of the sample charged to 2.2 V**

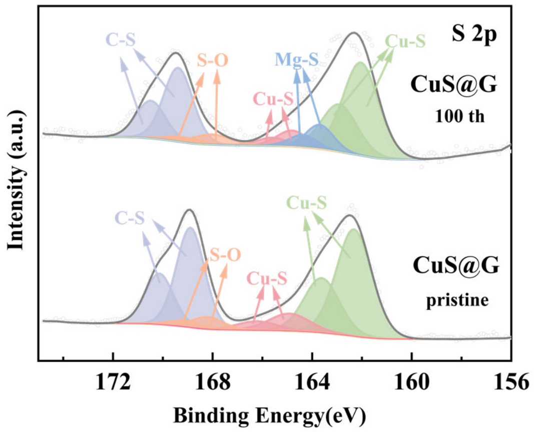

**Figure S21. XPS spectra of the S 2p region for the CuS@G electrode at 0 and 100 cycles.**

After 100 cycles, the S 2p spectrum of CuS@G still displays the peak corresponding to the C-S bond, with a slight shift towards higher binding energy, possibly due to interference from a small amount of unconverted $MgS_x$ on the material's surface (**Figure S21**). Furthermore, the dissolution of some polysulfides has slightly diminished the peak intensity, yet it remains clearly discernible. In summary, the persistence of the C-S bond after 100 cycles indicates robust long-term stability.

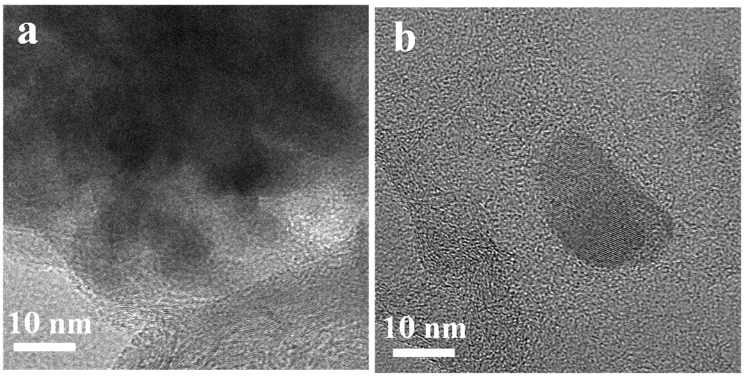

**Figure S22 TEM image of the first lap in a fully charged state of (a) CuS and (b) CuS@G.**

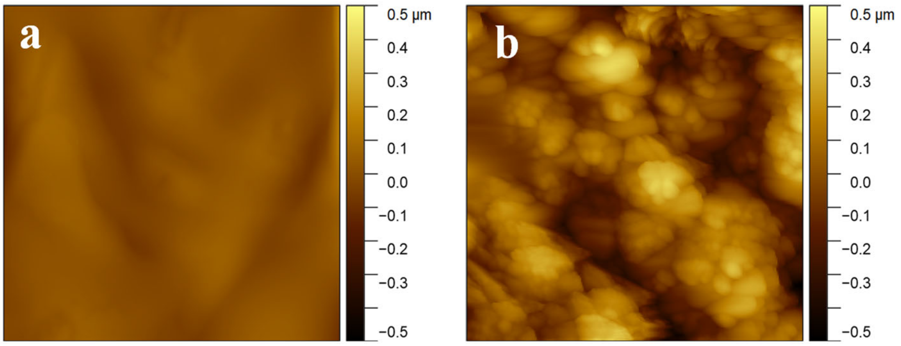

Figure S23 AFM images of (a)CuS and (b)CuS@G

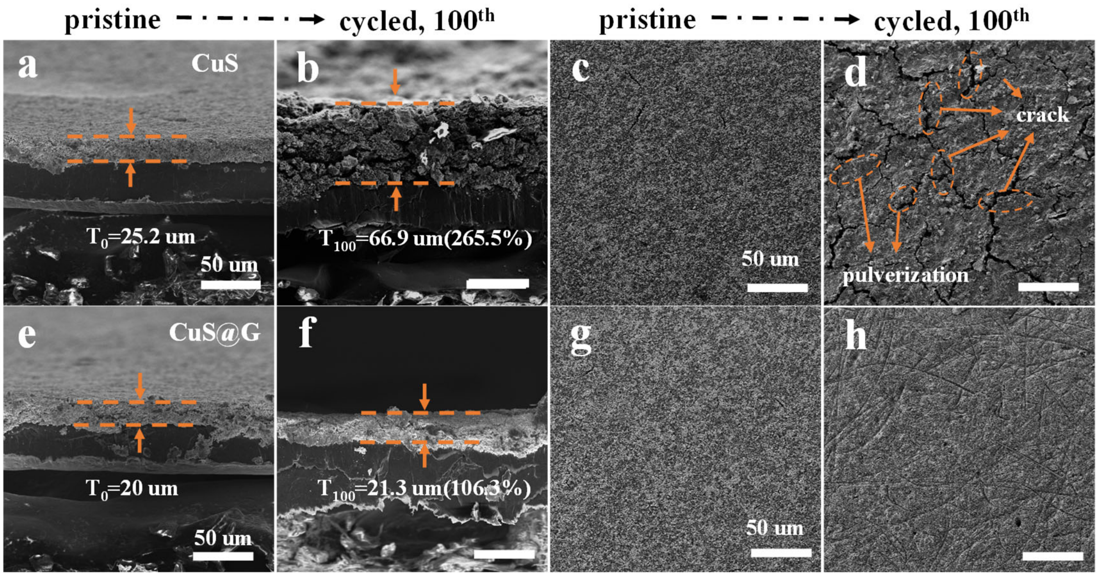

Figure S24 Characterization of the electrode after 100 cycles. Cross-sectional SEM images of (a) 0 and (b)100 cycles of the CuS electrode. Top-view SEM images of (c) 0 and (d)100 cycles of the CuS electrode. Cross-sectional SEM images of (e) 0 and (f)100 cycles of the CuS@G electrode. Top-view SEM images of (g) 0 and (h)100 cycles of the CuS@G electrode.

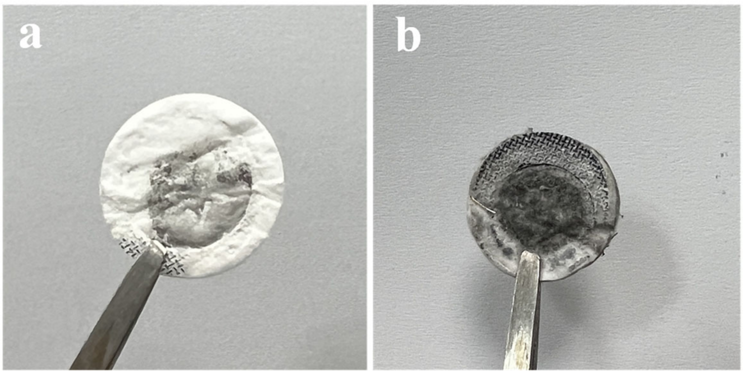

Figure S25 Optical image of the separator after 100 cycles of (a)CuS@G and (b)CuS.

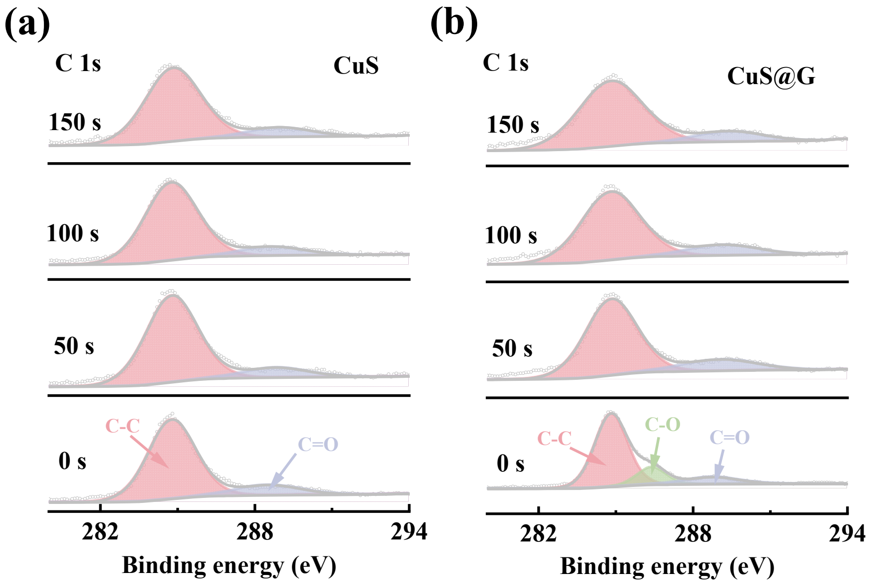

**Figure S26 The C 1s XPS spectra at different etching depths of Mg anodes after 100 cycles.**

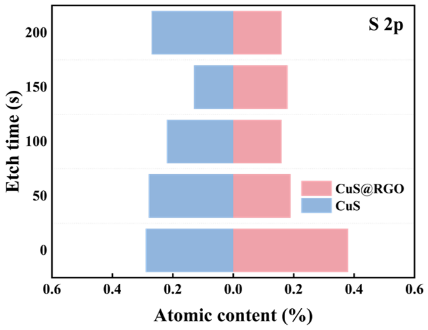

**Figure S27 S element content deposited on Mg anodes probed by XPS at different etch times.**

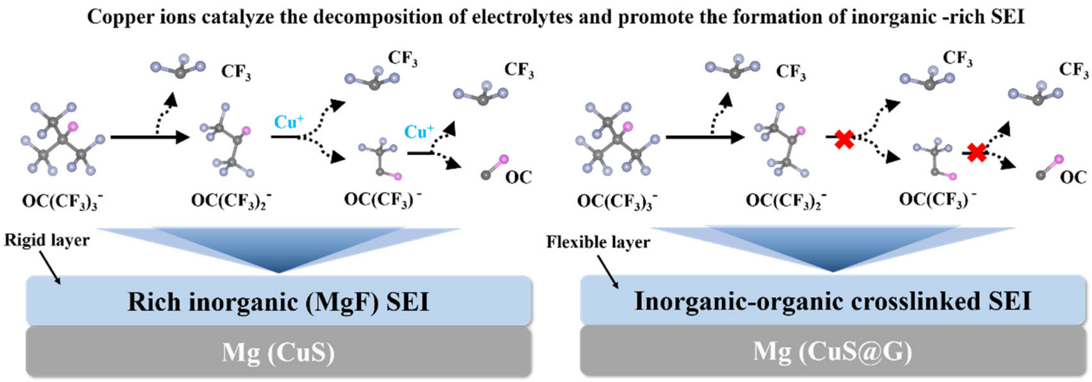

**Figure S28 Schematic diagram of copper ion catalytic electrolyte decomposition.**

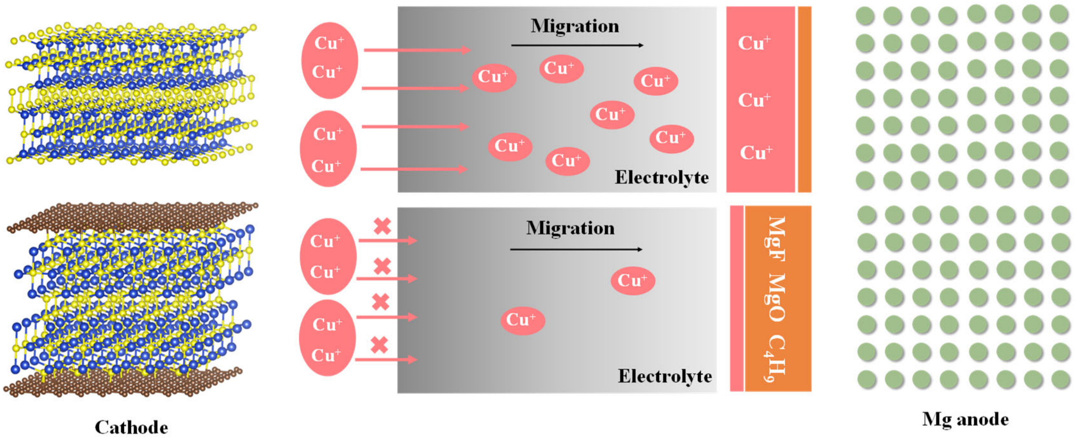

Figure S29 Schematic diagram of the effect of copper ion shuttle on the SEI of Mg anode.

Figure S30 The thickness of the Mg sheet used in pouch cells

Table S1 The results of the refinement of the pair distribution function.

| Sample | a (Å) | b (Å) | c (Å) |
|---|---|---|---|
| CuS | 3.797 | 3.797 | 16.497 |
| CuS@G | 3.802 | 3.802 | 16.491 |

**Table S2 The electrochemical properties of magnesium electrocathode materials have been reported.**[9–19]

| Sample | Capacity (50 mA $g^{-1}$) | Capacity (1000 mA $g^{-1}$) | Number of cycles | Reference |
|---|---|---|---|---|
| CuS@G | 287.5 | 164 | 1000 | This work |
| CuS NP | 175 | 90 | 350 | 9 |
| $VS_4$ | 177 | 104 | 800 | 10 |
| CuSSe | 225 | 100 | 200 | 11 |
| CuS NT | 210 | 140 | 600 | 12 |
| CuSe | 204 | 33.5 | 700 | 13 |
| $Cu_{2-x}Se$ | 210 | 100 | 300 | 14 |
| $CuCo_2S_4/Cu_{7.2}S_4$ | 256 | 123 | 300 | 15 |
| $Ti_3C_2/CoSe_2$ | 123 | 75.5 | 500 | 16 |
| $TiO_2$ | 150 | 80 | 1000 | 17 |
| $Co_{0.85}Se$ | 194 | 95 | 500 | 18 |
| $MoS_2$@G | 210 | 90 | 500 | 19 |

**Table S3 The ratio of $Cu^+$ and $Cu^{2+}$ in the sample at 2.2 V.**

| Sample | $Cu^+$ (Areal) | $Cu^+$ (%) | $Cu^{2+}$ (Areal) | $Cu^{2+}$(%) |
|---|---|---|---|---|
| CuS | 5831 | 66 | 3017 | 34 |
| CuS@G | 0 | 0 | 38961 | 100 |

**Table S4 ICP test of Mg anode after 100 cycles.**

| Sample | Spectral lines | Mass percentage |
|---|---|---|
| CuS | Mg 285.213 | 99.944% |
| | Cu 324.754 | 0.056% |
| CuS@G | Mg 285.213 | 99.986% |
| | Cu 324.754 | 0.014% |

## Reference

[1] W. Ren, F. Xiong, Y. Fan, Y. Xiong, Z. Jian, *ACS Appl. Mater. Interfaces* **2020**, *12*, 10471.

[2] J. Long, S. Tan, J. Wang, F. Xiong, L. Cui, Q. An, L. Mai, *Angew. Chem. Int. Ed.* **2023**, *62*, e202301934.

[3] G. Kresse, J. Furthmüller, *Phys. Rev. B* **1996**, *54*, 11169.

[4] G. Kresse, J. Hafner, *Phys. Rev. B* **1994**, *49*, 14251.

[5] J. P. Perdew, Y. Wang, *Phys. Rev. B* **1992**, *45*, 13244.

[6] G. Kresse, D. Joubert, *Phys. Rev. B* **1999**, *59*, 1758.

[7] S. Grimme, J. Antony, S. Ehrlich, H. Krieg, *J. Chem. Phys.* **2010**, *132*, 154104.

[8] K. Momma, F. Izumi, *J. Appl. Crystallogr.* **2008**, *41*, 653.

[9] M. Wu, Y. Zhang, T. Li, Z. Chen, S. Cao, F. Xu, *Nanoscale* **2018**, *10*, 12526.

[10] Y. Wang, Z. Liu, C. Wang, X. Yi, R. Chen, L. Ma, Y. Hu, G. Zhu, T. Chen, Z. Tie, J. Ma, J. Liu, Z. Jin, *Adv. Mater.* **2018**, *30*, 1802563.

[11] Z. Wang, Y. Zhu, C. Qiao, S. Yang, J. Jia, S. Rafai, X. Ma, S. Wu, F. Ji, C. Cao, *Small* **2019**, *15*, 1902797.

[12] C. Du, Y. Zhu, Z. Wang, L. Wang, W. Younas, X. Ma, C. Cao, *ACS Appl. Mater. Interfaces* **2020**, *12*, 35035.

[13] Y. Yang, J. Xiao, J. Cai, G. Wang, W. Du, Y. Zhang, X. Lu, C. C. Li, *Adv. Funct. Mater.* **2021**, *31*, 2005092.

[14] D. Chen, Y. Zhang, X. Li, J. Shen, Z. Chen, S. Cao, T. Li, F. Xu, *Chem. Eng. J.* **2020**, *384*, 123235.

[15] Q. Zhang, Y. Hu, J. Wang, Y. Dai, F. Pan, *Chem. – Eur. J.* **2021**, *27*, 13568.

[16] F. Liu, T. Wang, X. Liu, N. Jiang, L.-Z. Fan, *Chem. Eng. J.* **2021**, *426*, 130747.

[17] X. Cai, Y. Xu, Q. An, Y. Jiang, Z. Liu, F. Xiong, W. Zou, G. Zhang, Y. Dai, R. Yu, L. Mai, *Chem. Eng. J.* **2021**, *418*, 128491.

[18] D. Chen, F. Du, S. Cao, T. Li, F. Xu, *Chem. Eng. J.* **2022**, *428*, 129545.

[19] C. Wu, G. Zhao, X. Yu, C. Liu, P. Lyu, G. Maurin, S. Le, K. Sun, N. Zhang, *Chem. Eng. J.* **2021**, *412*, 128736.